

A novel heterozygous MAP2K1 mutation in a patient with Noonan syndrome with multiple lentigines.	Nishi E, Mizuno S, Nanjo Y, Niihori T, Fukushima Y, Matsubara Y, Aoki Y, Kosho T.	Am J Med Genet A.	167:407-11, 2015	国外
Mutations in PIGL in a patient with hyperphosphatasia mental retardation syndrome.	Fujiwara I, Murakami Y, Niihori T, Kanno J, Hakoda A, Sakamoto O, Okamoto N, Funayama R, Nagashima T, Nakayama K, Kinoshita T, Kure S, Matsubara Y, Aoki Y.	Am J Med Genet A	2015, in press	国外
Compound heterozygous deletions in pseudoautosomal region 1 in an infant with mild manifestations of Langer mesomelic dysplasia.	Tsuchiya T, Shibata M, Numabe H, Jinnno T, Nakabayashi K, Nishimura G, Nagai T, Ogata T, Fukami M*:	Am J Med Genet A	164A (2):505-510, 2014	国外
IMAGe syndrome: clinical and genetic implications based on investigations in three Japanese patients.	Kato F, Hamajima T, Hasegawa T, Amano N, Horikawa R, Nishimura G, Nakashima S, Fuke T, Sano S, Fukami M, Ogata T*:	Clin Endocrinol	80 (5):706-713, 2014	国外

<p>Japanese founder duplications/triplications involving BHLHA9 are associated with split-hand/foot malformation with or without long bone deficiency and Gallop-Wolfgang complex.</p>	<p>Nagata E, Kano H, Kato F, Yamaguchi R, Nakashima S, Takayama S, Kosaki R, Tonoki H, Mizuno S, Watanabe S, Yoshiura K, Kosho T, Hasegawa T, Kimizuka M, Suzuki A, Shimizu K, Ohashi H, Haga N, Numabe H, Horii E, Nagai T, Yoshihashi H, Nishimura G, Toda T, Takada S, Yokoyama S, Asahara H, Sano S, Fukami M, Ikegawa S, Ogata T*:</p>	<p>Orphanet J Rare Dis</p>	<p>9 (1):125, 2014</p>	<p>国外</p>
<p>De novo duplication of 17p13.1-p13.2 in a patient with intellectual disability and obesity.</p>	<p>Kuroda Y, Ohashi I, Tominaga M, Saito T, Nagai JI, Ida K, Naruto T, Masuno M, Kurosawa K.</p>	<p>Am J Med Genet A.</p>	<p>164A(6):1550-4,2014</p>	<p>国外</p>
<p>Early manifestations of BPAN in a pediatric patient</p>	<p>Okamoto N, Ikeda T, Hasegawa T, Yamamoto Y, Kawato K, Komoto T, Imoto I.</p>	<p>Am J Med Genet A</p>	<p>164A:3095-3099, 2014</p>	<p>国外</p>

Targeted next-generation sequencing in the diagnosis of neurodevelopmental disorders	Okamoto N, Miya F, Tsunoda T, Kato M, Saitoh S, Yamasaki M, Shimizu A, Torii C, Kanemura Y, Kosaki K.	Clin Genet	Epub ahead of print, 2015	国外
A clinical study of patients with pericentromeric deletion and duplication within 16p12.2-p11.2	Okamoto N, Fujii T, Tanaka J, Saito K, Matsui T, Harada N	Am J Med Genet A	164A:213-219, 2014	国外
De novo SOX11 mutations cause Coffin-Siris syndrome.	Tsurusaki Y, Koshimizu E, Ohashi H, Phadke S, Kou I, Shiina M, Suzuki T, Okamoto N, Imamura S, Yamashita M, Watanabe S, Yoshiura K, Kodera H, Miyatake S, Nakashima M, Saito H, Ogata K, Ikegawa S, Miyake N, Matsumoto N.	Nat Commun.	Jun 2;5:4011. doi: 10.1038/ncomms501, 2014.	国外

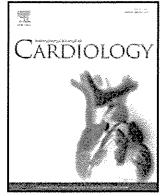
The spectrum of ZEB2 mutations causing the Mowat-Wilson syndrome in Japanese populations.	Yamada Y, Nomura N, Yamada K, Matsuo M, Suzuki Y, Sameshima K, Kimura R, Yamamoto Y, Fukushi D, Fukuhara Y, Ishihara N, Nishi E, Imataka G, Suzumura H, Hamano S, Shimizu K, Iwakoshi M, Ohama K, Ohta A, Wakamoto H, Kajita M, Miura K, Yokochi K, Kosaki K, Kuroda T, Kosaki R, Hiraki Y, Saito K, Mizuno S, Kurosawa K, Okamoto N, Wakamatsu N.	Am J Med Genet A.	164A(8):1899-908, 2014	国外
Microarray and FISH-based genotype-phenotype analysis of 22 Japanese patients with Wolf-Hirschhorn syndrome.	Shimizu K, Wakui K, Kosho T, Okamoto N, Mizuno S, Itomi K, Hattori S, Nishio K, Samura O, Kobayashi Y, Kako Y, Arai T, Tsutomu OI, Kawame H, Narumi Y, Ohashi H, Fukushima Y.	Am J Med Genet	164A:597-609, 2014	国外

Surgical intervention for esophageal atresia in patients with trisomy 18.	Nishi E, Takamizawa S, Iio K, Yamada Y, Yoshizawa K, Hatata T, Hiroma T, Mizuno S, Kawame H, Fukushima Y, Nakamura T, Kosho T.	Am J Med Genet A	164A:324-30, 2014	国外
【保護者への説明マニュアル】検査に対する説明マニュアル 遺伝子検査	川目 裕	小児科診療	2014	国内
【出生前診断を考える】出生前診断の遺伝カウンセリング	川目 裕	日本医師会雑誌	2014	国内

(注1) 発表者氏名は、連名による発表の場合には、筆頭者を先頭にして全員を記載すること。

(注2) 本様式は excel 形式にて作成し、甲が求める場合は別途電子データを納入すること。

IV. 研究成果の刊行物・別刷



Letter to the Editor

Bilateral giant coronary aneurysms in a 40-year-old male with Noonan syndrome caused by a *KRAS* germline mutation

Naoki Fujimoto^{a,*}, Hiroshi Nakajima^b, Emiyo Sugiura^b, Kaoru Dohi^b, Shinji Kanemitsu^c, Norikazu Yamada^b, Yoko Aoki^d, Kaname Nakatani^a, Hideto Shimpo^c, Tsutomu Nobori^a, Masaaki Ito^b

^a Department of Molecular and Laboratory Medicine, Mie University Graduate School of Medicine, Tsu, Japan

^b Department of Cardiology and Nephrology, Mie University Graduate School of Medicine, Tsu, Japan

^c Department of Thoracic and Cardiovascular Surgery, Mie University Graduate School of Medicine, Tsu, Japan

^d Department of Medical Genetics, Tohoku University School of Medicine, Sendai, Japan

ARTICLE INFO

Article history:

Received 7 February 2014

Accepted 15 March 2014

Available online 21 March 2014

Keywords:

Noonan syndrome

Coronary aneurysm

KRAS germline mutation

We report a case of a 40-year-old man who was admitted to our hospital for the evaluation and treatment of chest discomfort on exertion. He had previously been followed for post-natal growth deficiency, strabismus, mental retardation, epilepsy, and moderate mitral regurgitation. On admission, he was 142 cm in height and 42 kg in weight. Physical examination revealed orbital hypertelorism, ptosis, a webbed neck, and low-set ears with no jugular vein dilatation or peripheral edema. Cardiac auscultation showed a 3/6 late systolic murmur and S4. ECG showed normal sinus rhythm, poor R wave progression in the precordial leads, and an incomplete right bundle branch block. Chest X-ray showed pulmonary congestion and marked cardiomegaly, with a cardio-thoracic ratio of 71%.

Echocardiography revealed severe mitral regurgitation due to prolapse of the anterior and posterior mitral leaflets (Fig. 1A–C) and aneurysms near the left coronary artery (LCA) (Fig. 1D), and the right coronary artery (RCA). No left ventricular hypertrophy, wall motion abnormality, or atrial septal defects were observed. A CT scan also revealed coronary aneurysms with no pulmonic stenosis; one aneurysm near the LCA measured 40 × 32 mm, and the other near the RCA 13 × 12 mm (Fig. 2A–B). Total occlusion of right common iliac artery with subsequent aneurysmal change, and dilatation of left common iliac artery

were observed. Coronary angiography was then performed to elucidate the complex anatomy of the aneurysms and coronary arteries (Fig. 2C–D). A giant aneurysm containing a thrombus originated from the proximal LCA (Fig. 3 A–B). The left anterior descending artery was occluded with small collaterals from the left circumferential artery (LCX). The other aneurysm originated from the proximal RCA (Fig. 3 C–D), and the distal portion of the RCA was occluded with collaterals from the LCX.

It was thought that severe mitral regurgitation from a prolapsed leaflet and myocardial ischemia due to coronary aneurysms and severe occlusive coronary artery disease were responsible for his symptoms. The patient underwent a surgical procedure that involved mitral valve repair, ligation of the aneurysms, and coronary artery bypass grafting. The post-operative course was complicated by ventricular fibrillation during the operation and the patient unfortunately expired due to refractory congestive heart failure 13 days after surgery.

Genetic screening confirmed a heterozygous nucleotide change within exon 4b of the *KRAS* gene (c.458A>T), causing the amino acid substitution D153V, whose clinical phenotype was Noonan/Cardiofacio-cutaneous (CFC) syndrome [1,2].

Noonan syndrome was first described in 1963, and CFC syndrome was described in 1986. These syndromes have many overlapping manifestations such as short stature, characteristic facial appearance, mental retardation and heart abnormalities, including pulmonic stenosis, hypertrophic cardiomyopathy, and atrial septal defects. While, coronary aneurysms with occlusive coronary artery disease, as seen in our case, have been rarely reported in an adult patient with these syndromes [3]. Moreover, it was unclear when and how these cardiovascular changes had occurred during his life. We conclude that patients with Noonan/CFC syndrome may have the risks for coronary aneurysms and severe cardiovascular disease. Thus, careful cardiovascular follow-up should be performed in their entire life.

References

- [1] Schubert S, Zenker M, Rowe SL, et al. Germline *KRAS* mutations cause Noonan syndrome. *Nat Genet* 2006;38:331–6.
- [2] Niihori T, Aoki Y, Narumi Y, et al. Germline *KRAS* and *BRAF* mutations in cardio-facio-cutaneous syndrome. *Nat Genet* 2006;38:294–6.
- [3] Loukas M, Dabrowski M, Kantoch M, Ruzyllo W, Waltenberger J, Giannikopoulos P. A case report of Noonan's syndrome with pulmonary valvar stenosis and coronary aneurysms. *Med Sci Monit* 2004;10:CS80–3.

* Corresponding author at: Department of Molecular and Laboratory Medicine, Mie University Graduate School of Medicine, 2-174 Edobashi, Tsu 514-8507, Japan. Tel.: +81 59 231 5161; fax: +81 59 231 5250.

E-mail address: naokifujimo@clin.medic.mie-u.ac.jp (N. Fujimoto).

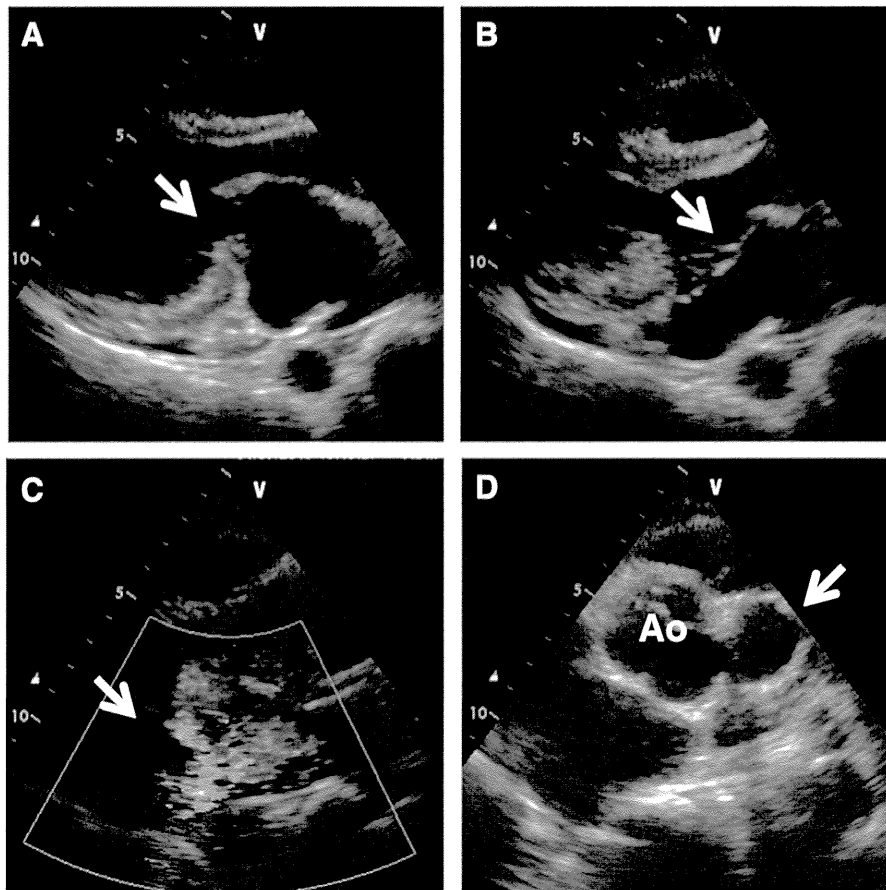


Fig. 1. Two-dimensional echocardiogram at end-diastole (A) and end-systole (B–C) showing severe mitral regurgitation due to mitral prolapse (arrow). Short axis image at the level of aortic valve with a giant aneurysm near left coronary artery (D).

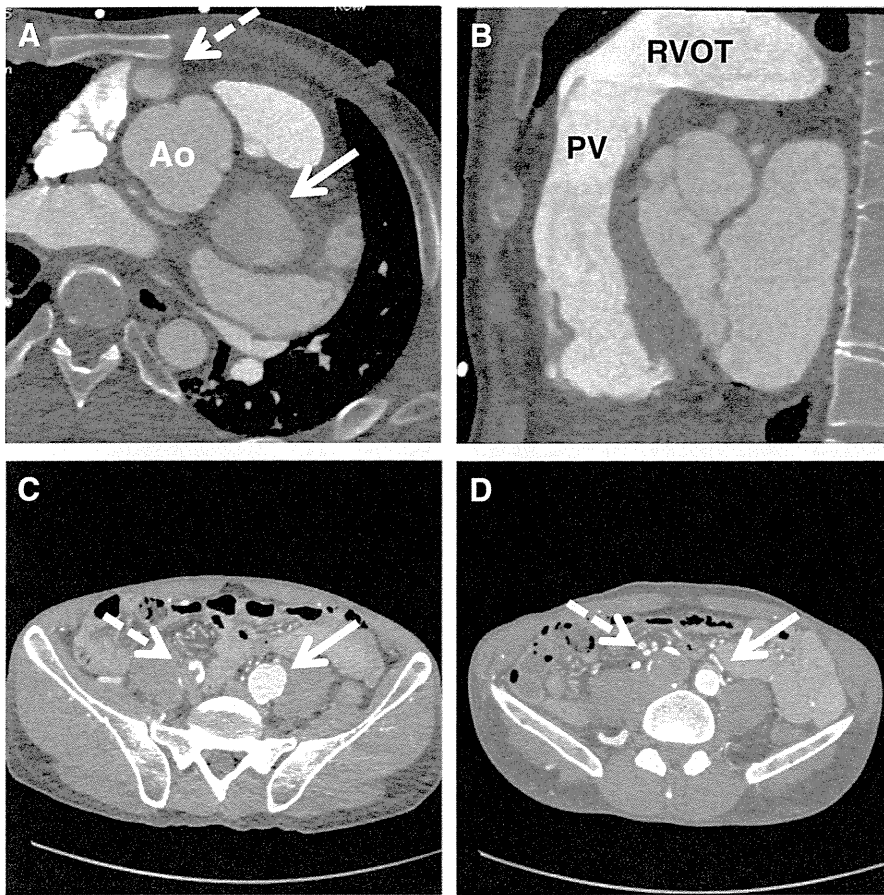


Fig. 2. Computed tomography (CT) axial view showing aneurysms near left coronary artery (arrow) and the right coronary artery (broken arrow)(A). CT sagittal view with intact pulmonic valve (PV) and right ventricular outflow tract (RVOT). CT axial view at proximal (C) and distal (D) levels of common iliac artery showing occluded right common iliac artery (broken arrow) and dilated left common iliac artery (arrow).

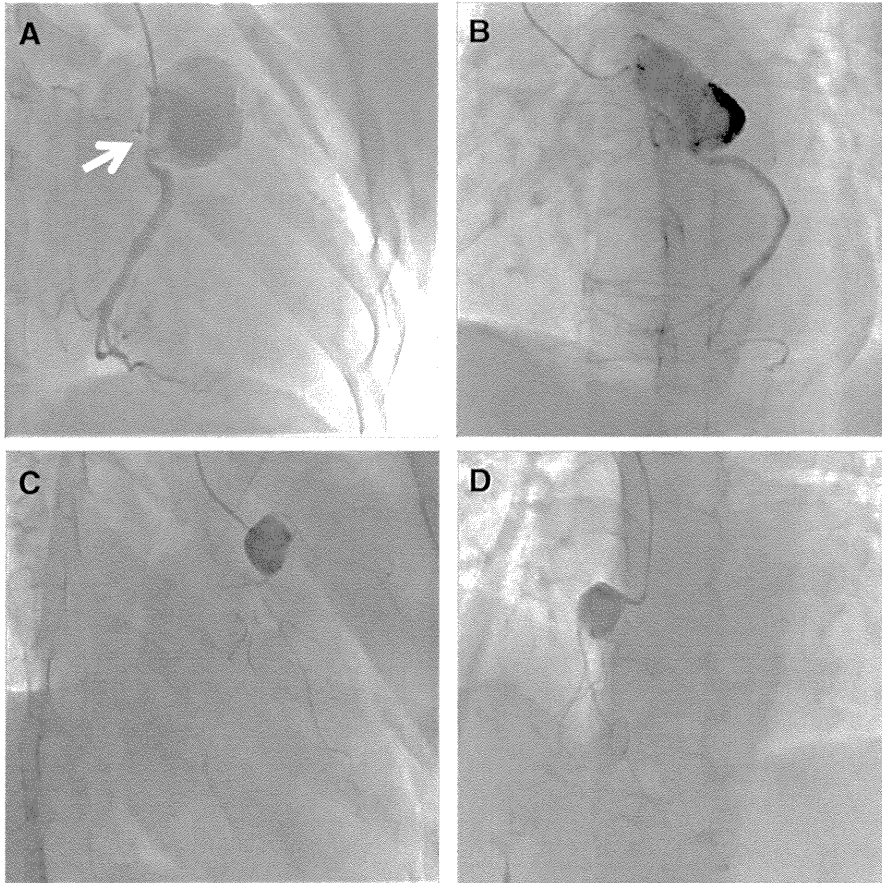


Fig. 3. Left coronary artery angiography in right anterior oblique (RAO; panel A) and left anterior oblique (LAO) views (panel B) showing a giant left coronary aneurysm containing a thrombus near the origin of the left circumflex coronary artery (arrow). Right coronary artery angiography in RAO caudal (C) and LAO cranial (D) views showing a right coronary aneurysm and coronary artery stenosis.

Activating mutations in *RRAS* underlie a phenotype within the RASopathy spectrum and contribute to leukaemogenesis

Elisabetta Flex^{1,†}, Mamta Jaiswal^{3,†}, Francesca Pantaleoni^{1,‡}, Simone Martinelli^{1,‡}, Marion Strullu^{4,7,‡}, Eyad K. Fansa^{3,‡}, Aurélie Caye^{4,7}, Alessandro De Luca⁸, Francesca Lepri⁹, Radovan Dvorsky³, Luca Pannone¹, Stefano Paolacci¹, Si-Cai Zhang³, Valentina Fodale¹, Gianfranco Bocchinfuso¹⁰, Cesare Rossi¹¹, Emma M.M. Burkitt-Wright¹², Andrea Farrotti¹⁰, Emilia Stellacci¹, Serena Cecchetti², Rosangela Ferese⁸, Lisabianca Bottero¹, Silvana Castro¹³, Odile Fenneteau⁵, Benoît Brethon⁶, Massimo Sanchez², Amy E. Roberts¹⁴, Helger G. Yntema¹⁵, Ineke Van Der Burgt¹⁵, Paola Cianci¹⁶, Marie-Louise Bondeson¹⁷, Maria Cristina Digilio⁹, Giuseppe Zampino¹⁸, Bronwyn Kerr¹², Yoko Aoki¹⁹, Mignon L. Loh²⁰, Antonio Palleschi¹⁰, Elia Di Schiavi^{13,¶}, Alessandra Carè¹, Angelo Selicorni¹⁶, Bruno Dallapiccola⁹, Ion C. Cirstea^{3,21}, Lorenzo Stella¹⁰, Martin Zenker²², Bruce D. Gelb^{23,24,25}, Hélène Cavé^{4,7,§}, Mohammad R. Ahmadian^{3,§} and Marco Tartaglia^{1,§,*}

¹Dipartimento di Ematologia, Oncologia e Medicina Molecolare and ²Dipartimento di Biologia Cellulare e Neuroscienze, Istituto Superiore di Sanità, Rome 00161, Italy, ³Institut für Biochemie und Molekularbiologie II, Medizinische Fakultät der Heinrich-Heine Universität, Düsseldorf 40225, Germany, ⁴Genetics Department, ⁵Biological Hematology Department and ⁶Pediatric Hematology Department, Robert Debré Hospital, Paris 75019, France, ⁷INSERM UMR_S940, Institut Universitaire D'Hématologie (IUH), Université Paris-Diderot Sorbonne-Paris-Cité, Paris 75010, France, ⁸Laboratorio Mendel, Istituto di Ricovero e Cura a Carattere Scientifico-Casa Sollievo Della Sofferenza, Rome 00198, Italy, ⁹Ospedale Pediatrico 'Bambino Gesù', Rome 00165, Italy, ¹⁰Dipartimento di Scienze e Tecnologie Chimiche, Università 'Tor Vergata', Rome 00133, Italy, ¹¹UO Genetica Medica, Policlinico S.Orsola-Malpighi, Bologna 40138, Italy, ¹²Genetic Medicine, Academic Health Science Centre, Central Manchester University Hospitals NHS Foundation Trust, Manchester M13 9WL, UK, ¹³Istituto di Genetica e Biofisica 'A. Buzzati Traverso', Consiglio Nazionale Delle Ricerche, Naples 80131, Italy, ¹⁴Department of Cardiology and Division of Genetics, and Department of Medicine, Boston Children's Hospital, Boston, MA 02115, USA, ¹⁵Department of Human Genetics, Radboud University Medical Centre, and Nijmegen Centre for Molecular Life Sciences, Radboud University, Nijmegen 6500, The Netherlands, ¹⁶Genetica Clinica Pediatrica, Clinica Pediatrica Università Milano Bicocca, Fondazione MBBM, A.O. S. Gerardo, Monza 20900, Italy, ¹⁷Department of Immunology, Genetics and Pathology, Uppsala University, Uppsala 75237, Sweden, ¹⁸Istituto di Clinica Pediatrica, Università Cattolica del Sacro Cuore, Rome 00168, Italy, ¹⁹Department of Medical Genetics, Tohoku University School of Medicine, Sendai 980-8574, Japan, ²⁰Department of Pediatrics, Benioff Children's Hospital, University of California School of Medicine, and the Helen Diller Family Comprehensive Cancer Center, San Francisco, CA 94143, USA, ²¹Leibniz Institute for Age Research, Jena 07745, Germany, ²²Institute of Human Genetics, University Hospital of

*To whom correspondence should be addressed at: Dipartimento di Ematologia, Oncologia e Medicina Molecolare, Istituto Superiore di Sanità, Viale Regina Elena, 299, 00161 Rome, Italy. Tel: +39 0649902569; Fax: +39 0649902850; Email: marco.tartaglia@iss.it

[†]These authors contributed equally to this project.

[‡]These authors contributed equally to this project.

[¶]Present address: Institute of Bioscience and BioResources, Consiglio Nazionale delle Ricerche, Naples 80131, Italy.

[§]These authors contributed equally as the senior investigators for this project.

© The Author 2014. Published by Oxford University Press.

This is an Open Access article distributed under the terms of the Creative Commons Attribution Non-Commercial License (<http://creativecommons.org/licenses/by-nc/4.0/>), which permits non-commercial re-use, distribution, and reproduction in any medium, provided the original work is properly cited. For commercial re-use, please contact journals.permissions@oup.com

Magdeburg, Otto-von-Guericke-University, Magdeburg 39120, Germany, ²³Department of Pediatrics and ²⁴Department of Genetics and ²⁵Department of Genomic Sciences, Mindich Child Health and Development Institute, Icahn School of Medicine at Mount Sinai, New York, NY 10029, USA

Received December 10, 2013; Revised and Accepted March 4, 2014

RASopathies, a family of disorders characterized by cardiac defects, defective growth, facial dysmorphism, variable cognitive deficits and predisposition to certain malignancies, are caused by constitutional dysregulation of RAS signalling predominantly through the RAF/MEK/ERK (MAPK) cascade. We report on two germline mutations (p.Gly39dup and p.Val55Met) in *RRAS*, a gene encoding a small monomeric GTPase controlling cell adhesion, spreading and migration, underlying a rare (2 subjects among 504 individuals analysed) and variable phenotype with features partially overlapping Noonan syndrome, the most common RASopathy. We also identified somatic *RRAS* mutations (p.Gly39dup and p.Gln87Leu) in 2 of 110 cases of non-syndromic juvenile myelomonocytic leukaemia, a childhood myeloproliferative/myelodysplastic disease caused by upregulated RAS signalling, defining an atypical form of this haematological disorder rapidly progressing to acute myeloid leukaemia. Two of the three identified mutations affected known oncogenic hotspots of *RAS* genes and conferred variably enhanced *RRAS* function and stimulus-dependent MAPK activation. Expression of an *RRAS* mutant homolog in *Caenorhabditis elegans* enhanced RAS signalling and engendered protruding vulva, a phenotype previously linked to the RASopathy-causing *SHOC2*^{S2G} mutant. Overall, these findings provide evidence of a functional link between *RRAS* and MAPK signalling and reveal an unpredicted role of enhanced *RRAS* function in human disease.

INTRODUCTION

Signalling elicited by activated cell surface receptors and transduced through RAS proteins to the RAF/MEK/ERK and PI3K/AKT cascades is central to cell proliferation, survival, differentiation and metabolism (1,2). Owing to this nodal role, enhanced traffic through RAS proteins and their downstream effectors has been established to have a major impact on oncogenesis (3,4). This signalling network also controls early and late developmental processes (e.g. organogenesis, morphology determination, synaptic plasticity and growth), and germline mutations in a number of genes encoding transducers and modulatory proteins participating in the RAS/MAPK signalling pathway have been causally linked to Noonan syndrome (NS) (5), one of the most common diseases affecting development and growth, and a group of clinically related syndromes, the so-called RASopathies (6–8). In this family of disorders, constitutional dysregulation of RAS signalling can be caused by enhanced activation of *HRAS*, *KRAS* and *NRAS* (RAS proteins hereafter), aberrant function of upstream signal transducers or effectors (*PTPN11*/*SHP2*, *SOS1*, *SHOC2*, *RAF1*, *BRAF*, *MAP2K1*/*MEK1* and *MAP2K2*/*MEK2*) or inefficient down modulation by feedback mechanisms (*CBL*, *NF1* and *SPRED1*). More recently, *RIT1*, encoding a monomeric GTPase structurally linked to RAS proteins, was identified as disease gene implicated in NS (9), extending the concept of ‘RASopathy gene’ to a transducer that contributes to signal propagation through RAS effector pathways but does not belong to the RAS/MAPK signalling backbone.

Clinical manifestations of RASopathies include postnatal reduced growth, a wide spectrum of cardiac defects, facial dysmorphism, ectodermal and skeletal anomalies and variable

cognitive deficits (5,8,10). Consistent with the key role of most RASopathy genes in oncogenesis, these disorders are also characterized by variably increased risk for certain haematologic malignancies and other paediatric cancers (6,7,11,12). Most of these conditions are genetically heterogeneous, and the underlying disease gene has not been identified yet for a still significant fraction of cases. Based on the strict mechanistic link between the molecular events controlling development and contributing to oncogenesis, these ‘missing’ genes represent excellent candidate oncogenes/tumour suppressors.

Here, we report that constitutional dysregulation of *RRAS* function is associated with a Mendelian trait within the RASopathy spectrum and that somatically acquired mutations in the same gene occur in an aggressive form of juvenile myelomonocytic leukaemia (JMML), a rare childhood myeloproliferative/myelodysplastic neoplasm representing the archetypal somatic RASopathy (13), rapidly progressing to acute myeloid leukaemia (AML). We also demonstrate that RASopathy-causing *RRAS* mutations are activating and promote signalling perturbation by enhancing stimulus-dependent MEK, ERK and, at a lower extent, AKT phosphorylation.

RESULTS

Identification of candidate disease genes and *RRAS* mutation analysis

While the core of the machinery implicated in RAS signalling has been characterized comprehensively, signal propagation through this network is likely to include a larger number of proteins playing a modulatory or structural role (14), whose aberrant or defective function is expected to perturb development and

contribute to oncogenesis. Based on this assumption, we used a protein interaction/functional association network analysis to select a panel of genes encoding proteins functionally linked to the RAS signalling network as candidates for NS or a related RASopathy (15). Candidate gene selection was based on the use of the previously identified RASopathy genes as 'seed' proteins (i.e. proteins used to build the interaction/functional networks), and considering a panel of databases to construct functional subnetworks (Supplementary material, Table S1 and Fig. S1). Sequence scanning of the best candidates in a RASopathy cohort including 96 unrelated subjects negative for mutations in known disease genes allowed the identification of a functionally relevant *RRAS* change (c.163G>A, p.Val55Met) (Supplementary material, Fig. S2) in an adult subject with clinical features suggestive of NS but lacking sufficient characteristics to allow a definitive diagnosis (Supplementary material, Table S2). Parental DNA was not available for segregation analysis. The mutation was not identified among >400 population-matched unaffected individuals, indicating that it did not represent a common polymorphic nucleotide substitution. This change, rs368625677 (dbSNP 138), had been described in 1/13,006 alleles in the NHLBI Exome Sequencing Project (<http://eversusgs.washington.edu/EVS/>). Of note, similar frequencies have been reported in the same database for recurrent RASopathy-causing mutations (e.g. c.922A>G in *PTPN11*, and c.1259G>A in *CBL*). Mutation analysis was extended to additional 408 patients with NS or a clinically related phenotype tested negative for mutations in the major NS disease genes (see Materials and Methods), allowing to identify one sporadic case heterozygous for a three-nucleotide duplication (c.116_118dup, p.Gly39dup) (Supplementary material, Fig. S2). Parental DNA sequencing of the relevant exon demonstrated the *de novo* origin of the variant, and STR genotyping confirmed paternity. In this subject, the duplication was documented in DNA obtained from skin fibroblasts, excluding a somatic event restricted to haematopoietic cells. The subject had features reminiscent of NS (Fig. 1A and Supplementary material, Table S2), with onset of AML suspected to represent a blast crisis of JMML (Supplementary material, Table S3 and Fig. S3). In this patient, exome sequencing performed on leukaemic and non-leukaemic DNA failed to disclose any additional relevant germline/somatic change affecting genes known to be mutated in RASopathies and JMML, as well as genes directly linked to the RAS signalling network, further supporting the causal role of the identified *RRAS* lesion. Based on this association, the occurrence of *RRAS* mutations was also explored in a panel of genomic DNAs obtained from bone marrow aspirates/circulating leukocytes of 110 subjects with JMML. Heterozygosity for the previously identified Gly³⁹ duplication and the c.260A>T (p.Gln87Leu) change was observed in two patients with JMML rapidly progressing to AML (Supplementary material, Table S3 and Fig. S3). Both lesions were absent in non-leukaemic DNA, indicating their somatic origin (Supplementary material, Fig. S2). These subjects also carried a somatic *NRAS* mutation, suggesting that the two hits might cooperate with this particularly severe form of disease. Sequencing of isolated JMML myeloid colonies in patient 14385 showed that *NRAS* and *RRAS* mutations coexisted in the same progenitors but failed to establish their sequence of appearance during leukaemogenesis, not allowing to discriminate whether the latter was involved in initiation or progression of disease.

Structural analyses

RRAS encodes a 23-kD a membrane-bound monomeric GTPase with 55–60% amino acid identity to RAS proteins (16). This highly conserved structure is flanked by a unique 26-amino acid region at the *N*-terminus (Fig. 1B). Similarly to the other RAS family proteins, *RRAS* binds to GTP and GDP with high affinity and specificity and functions as a molecular switch by cycling between active, GTP-bound and inactive, GDP-bound states (17). *RRAS* is activated by guanine nucleotide exchange factors (GEFs) in response to signals elicited by cell surface receptors. In the GTP-bound state, two functionally conserved regions, switch I and switch II (Fig. 1B), undergo a conformational change enabling *RRAS* to bind to and activate effector proteins. This interaction is terminated by hydrolysis of GTP to GDP, which is promoted by GTPase-activating proteins (GAPs) and results in switching towards the inactive conformation. Disease-associated *RRAS* mutations affected residues highly conserved among orthologs and paralogs (Supplementary material, Fig. S4) residing in the GTP-binding pocket (Fig. 1C) and were predicted to be damaging with high confidence (Supplementary material, Table S4). Among them, Gln⁸⁷, homolog of Gln⁶¹ in RAS proteins, is directly involved in catalysis (18,19). The p.Gln87Leu substitution had previously been reported as a rare somatic event in lung carcinoma, and mutations affecting Gln⁶¹ are among the most recurrent oncogenic lesions in *RAS* genes (COSMIC database, <http://cancer.sanger.ac.uk/cancergenome/projects/cosmic/>). Likewise, p.Gly39dup altered the G1 motif participating in GTP/GDP binding and GTPase activity (Fig. 1B). Within this motif, Gly¹² and Gly¹³ (Gly³⁸ and Gly³⁹ in *RRAS*) represent major mutation hot-spots in human cancer (COSMIC database) and account for the majority of germline *HRAS* mutations causing Costello syndrome (20). Of note, analogous insertions in RAS proteins have been reported in JMML and other malignancies (21–24). In contrast, no somatic/germline *RAS* mutation affecting Val²⁹, homolog of Val⁵⁵ in *RRAS*, had previously been reported. Val⁵⁵ side-chain is not directly involved in GTP/GDP binding, GTP hydrolysis or interaction with effectors. However, it has been reported that H-bonds are possible between the backbone of Val²⁹ in *HRAS* and GDP/GTP (25). Furthermore, it has been suggested that Val²⁹ can play a role in the transition between the GDP- and GTP-bound states (26), as supported by the evidence that the Val29Gly substitution in *HRAS* accelerates the GDP/GTP exchange *in vitro* (27).

Molecular dynamics (MD) simulations were performed to predict *in silico* the effects of p.Val55Met on the structure and dynamics of *RRAS* (Fig. 2). The mutation was introduced in the available crystallographic structure of *RRAS* in complex with GDP and Mg²⁺, and the system was simulated in water for 200 ns. For comparison, MD simulations were also performed using the wild-type protein, which maintained a stable structure along the whole simulation, as expected (Fig. 2A, left panel). In contrast, a dramatic local structural transition extending up to the switch I region (residues 58–64), which mediates effector binding, was documented for the *RRAS*^{V55M} mutant, after ~80 ns (Fig. 2A, right panel). This conformational transition resulted in an increased solvent exposure of Met⁵⁵, in agreement with the higher hydrophilicity of this residue compared with Val, and was accompanied by the formation of a stable

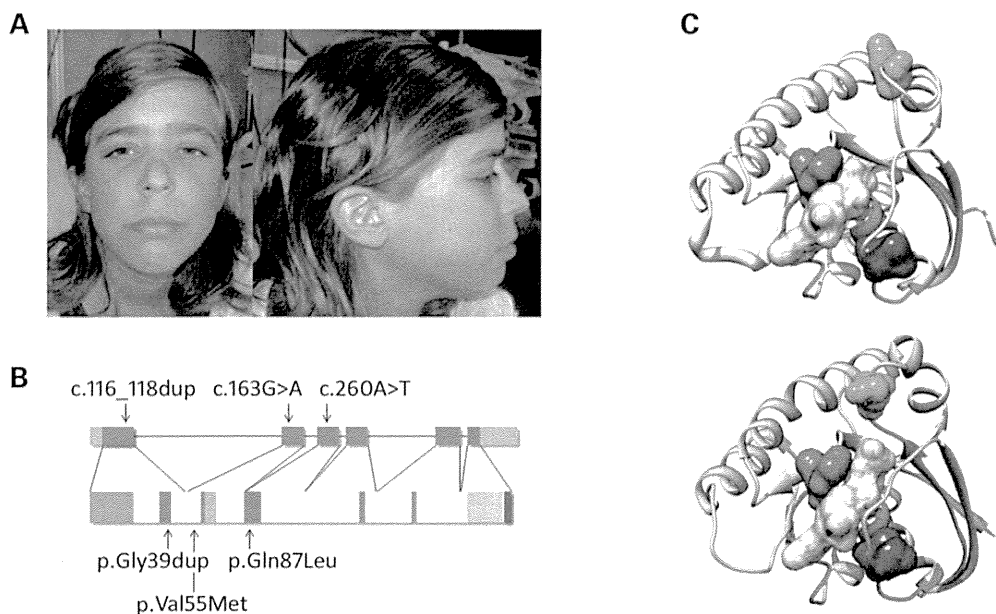


Figure 1. RASopathy-causing and leukaemia-associated *RRAS* mutations. (A) Facial features of the affected subject (9802) heterozygous for the *de novo* germline c.116_118dup. (B) *RRAS* exon–intron arrangement with coding exons as blue boxes. *RRAS* functional motifs include the GTP/GDP binding domain (G1 to G5, starting from the *N*-terminus) (red), switch I (light green), switch II (dark green) and hypervariable region (light brown) with the C-terminal CAAX motif (dark brown). The unique *N*-terminal region is also shown (violet). Location of disease-associated mutations is reported. (C) Position of affected residues on the three-dimensional structure of *RRAS* in its GDP-bound, inactive state (PDB: 2FN4) (above) and that of non-hydrolysable GTP analogue (GppNHp)-bound, active HRAS (PDB: 5P21) (below). The red surface indicates Gly³⁹ and Val⁴⁰ (Gly¹³ and Val¹⁴, in HRAS), whereas Val⁵⁵ (Val²⁹) and Gln⁸⁷ (Gln⁶¹) are shown in blue and green, respectively. GDP is reported as semi-transparent yellow surface.

cluster involving residues Ile⁵⁰, Met⁵⁵ and Tyr⁵⁸ (Fig. 2A and Supplementary material, Table S5) permitted by the unbranched and long side-chain of Met⁵⁵. No further significant conformational changes were observed for the remaining interval of the simulation. The major effect of this structural rearrangement was to increase exposure of GDP to the solvent (Fig. 2B), with an almost doubled solvent accessible surface area of the nucleotide after the conformational transition. This structural rearrangement was accompanied by a perturbation of the intermolecular H-bond network stabilizing GDP binding, with loss of the H-bonds between residues at codons 55 and 56, and GDP (Supplementary material, Table S5). Of note, a possible impact of the described structural transition on *RRAS* binding to GEF proteins, which bind to this region and mediate GDP release, was also noticed. Specifically, we observed that after the conformational rearrangement, the *RRAS*^{V55M} region implicated in GEF binding populated a structure similar to that assumed in *RAS*/GEF complexes (Fig. 2C), suggesting a possible enhanced interaction of the disease-associated *RRAS* mutant with GEFs. In particular, Tyr⁵⁸ was observed to adopt a side-chain orientation very similar to that of the *RAS* homolog Tyr³² in the *HRAS*/*SOS1* complex, which has been shown to contribute to the structural rearrangements of switch I and interaction with GEFs (28–30).

Overall, these data supported an activating role of p.Val55Met through enhanced GDP release as a result of a decreased affinity for the nucleotide and/or enhanced interaction with a GEF.

Biochemical and functional characterization of *RRAS* mutants

Previous studies documented the gain-of-function role of p.Gln87Leu on *RRAS* function, and MAPK and PI3K/AKT signalling (31). To characterize the impact of p.Val55Met and p.Gly39dup on protein function, we analysed the intrinsic and GEF-accelerated nucleotide exchange reaction of these mutants. Dissociation kinetics analysis demonstrated a dramatically increased intrinsic (*RRAS*^{G39dup}) and GEF-stimulated (*RRAS*^{G39dup} and *RRAS*^{V55M}) dissociation rate of mantGDP, indicating a facilitated nucleotide release in both mutants (Fig. 3A). *RAS* proteins exhibit low intrinsic GTPase activity that is enhanced by GAPs (32). Assessment of *RRAS*^{G39dup} and *RRAS*^{V55M} GTPase activity documented a significantly reduced intrinsic and GAP-stimulated GTP hydrolysis in the former (Fig. 3B and Supplementary material, Fig. S5). Finally, the interaction of *RRAS* proteins with various effectors was analysed by fluorescence polarization (Fig. 3C). While *RRAS*^{WT} was found to bind to RAF1, RALGDS, RASSF5 and PLCE1 less efficiently than *HRAS*, an increased binding affinity to PIK3CA was observed. Compared with *RRAS*^{WT}, aberrant binding behaviour of the two *RRAS* mutants was demonstrated, with *RRAS*^{G39dup} exhibiting an increased binding affinity towards PIK3CA, RAF1, PLCE1 and RASSF5, and *RRAS*^{V55M} to RALGDS.

To gain further insights into the impact of disease-causing mutations on *RRAS* functional dysregulation and explore their effects on *RAS* signalling, the activation state of *RRAS* proteins

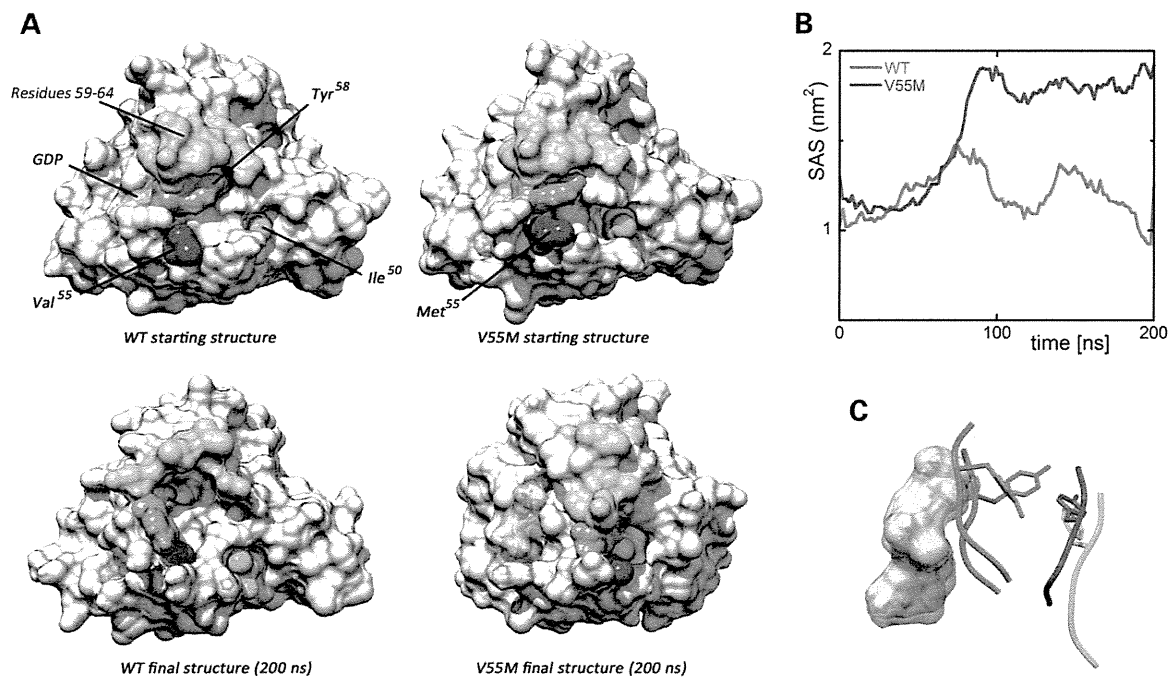


Figure 2. Molecular dynamics (MD) simulations. (A) Structural perturbations promoted by the p.Val55Met substitution as obtained from MD simulations of the RRAS/GDP complex. The wild-type (WT) protein is also shown for comparison. Top panels report the protein structures at the beginning of simulations, whereas the final structures (200 ns) are shown at the bottom. The final structure of RRAS^{V55M} is well representative of the last 120 ns of the trajectory. The protein surface of RRAS is shown with GDP (yellow). The mutated residues and those forming a cluster in the simulation of mutated RRAS are coloured as follows: Val⁵⁵/Met⁵⁵ (blue), Tyr⁵⁸ (pink) and Ile⁵⁰ (cyan). Residues 59–64, which, together with Tyr⁵⁸, form the switch I region, are coloured in green. (B) Solvent accessible surface of GDP in the MD simulations of wild-type (red) and mutant (blue) RRAS/GDP complexes. (C) Conformation of the loop comprised between Val⁵⁵/Met⁵⁵ and Asp⁵⁹ in wild-type (red) and mutant (blue) RRAS/GDP complexes obtained from MD simulations. GDP is reported as semi-transparent yellow surface. Superimposed conformations of the corresponding loop (residues 29–33) in GDP-bound HRAS (violet) (PDB: 4Q21) and GDP-bound HRAS complexed with SOS1 (cyan) (PDB: 1BKD) are shown for comparison. The side chains of Tyr⁵⁸ and the corresponding residue in HRAS, Tyr³², are displayed as sticks.

and extent of signalling through the MAPK and PI3K/AKT cascades were evaluated using transient expression in COS-7 cells. Consistent with the above-mentioned findings, pull-down assays revealed a variably higher proportion of active, GTP-bound form for both mutants (Fig. 4A). Moreover, similarly to what observed under cell-free conditions, RRAS^{G39dup} was resistant to GAP stimulation. Expression of both mutants promoted enhanced serum-dependent MEK, ERK and AKT phosphorylation (Fig. 4B), which was more evident in cells expressing the RRAS^{G39dup} mutant.

Caenorhabditis elegans studies

To explore further the functional impact of the RASopathy causative RRAS mutants on RAS signalling *in vivo*, we used the nematode *C. elegans* as an experimental model. In *C. elegans*, the role of *ras-1*, the RRAS ortholog (33), has not been characterized yet. On the contrary, proper signalling through LET-60, the *C. elegans* ortholog of RAS proteins, has been established to play a crucial role in vulval development (34). In particular, LET-60/RAS is known to mediate the priming signal (LIN-3/EGF) released by the anchor cell to induce the three nearby vulval precursor cells (VPCs), P5.p, P6.p and P7.p, to generate a normal vulva. Enhanced and decreased signalling through LET-60 and the MAPK cassette

results in multiple ectopic pseudovulvae (multivulva phenotype) and a failure in VPC induction (vulvaless phenotype), respectively (34,35).

Multiple transgenic lines were generated to conditionally express the wild-type *ras-1* cDNA (*ras-1*^{WT}) or the allele homologous to the disease-associated three-nucleotide duplication (*ras-1*^{G27dup}), which was identified to occur both as a germline and somatic event. Exogenous RAS-1 expression was induced by heat shock at early L3 larval stage to investigate the effects of the mutant protein on vulval development. Animals expressing *ras-1*^{G27dup} displayed abnormal vulval morphogenesis resulting in the formation of a protruding vulva (Pvl) (Fig. 5A and B and Supplementary Material, Table S6), a phenotype associated with aberrant traffic through different signalling cascades (36,37). Of note, this phenotype had previously been reported in worms expressing the RASopathy causative SHOC2^{S2G} mutant (38). Like those animals, *ras-1*^{G27dup} worms showed decreased egg-laying efficiency (Egl phenotype), and accumulation of larvae inside the mother (Bag-of-worms phenotype). A significantly less penetrant phenotype was observed in animals expressing *ras-1*^{WT}. These findings, together with the observation that animals lacking *ras-1* do not exhibit any vulval defect (WormBase, <http://www.wormbase.org/>, and our personal assessment), supported the gain-of-function role of the mutation on RAS-1 function. At the late L3/early L4 larval stage, vulva

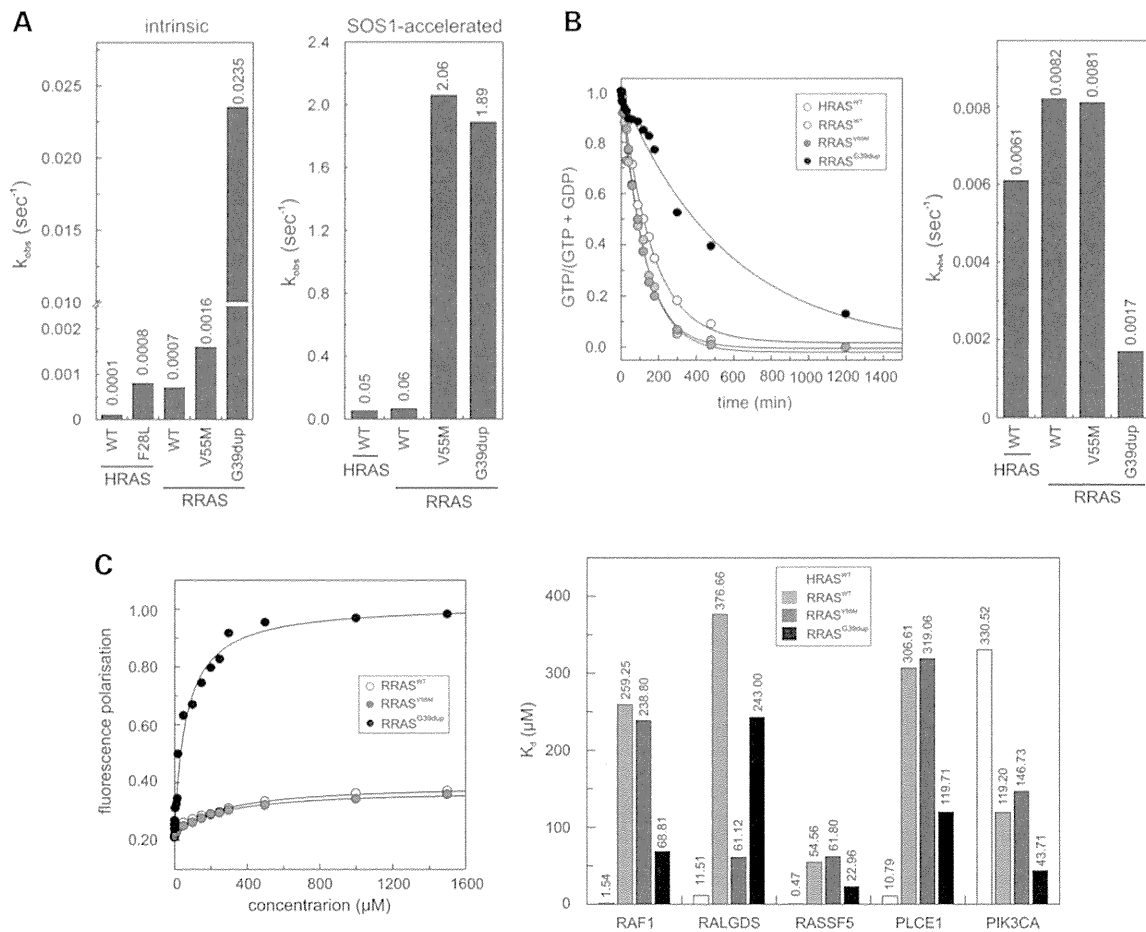


Figure 3. *In vitro* biochemical characterization of the RRAS^{G39dup} and RRAS^{V55M} mutants. (A) Intrinsic (left) and SOS1-accelerated (right) mantGDP nucleotide dissociation measured in the presence of 20-fold excess of non-labelled GDP. The decrease in mant fluorescence was fitted by single exponentials to obtain k_{obs} values for nucleotide dissociation. RRAS^{G39dup} exhibited a 35-fold increased intrinsic dissociation of mantGDP, whereas SOS1-accelerated mantGDP dissociation was augmented by ~30-fold for both mutants, compared with RRAS^{WT} and HRAS^{WT}. The k_{obs} values are an average of five to seven independent measurements. (B) Intrinsic GTP hydrolysis kinetics (left) and rate constants (right) of RRAS^{G39dup} and RRAS^{V55M} proteins, documenting the impaired catalytic activity in the former. The k_{obs} values are an average of five to seven independent measurements. (C) Binding of RRAS^{WT}, RRAS^{V55M} and RRAS^{G39dup} to the RAS-binding domain of RAF1 measured as variation in fluorescence polarization of each mantGppNHp-bound RRAS protein at increasing concentrations of RAF1-RBD (left), and dissociation constants (K_d) for the interaction of HRAS^{WT} and RRAS proteins to the RBDs of RAF1, RALGDS, PLCE1, PIK3CA and RASSF5 (right). K_d values were obtained by quadratic fitting of the concentration-dependent binding curves from fluorescence polarization measurement as exemplified for RAF1-RBD. Of note, RRAS^{WT} binds to RAF1, RALGDS, RASSF5 and PLCE1 less efficiently than HRAS, whereas an increased binding affinity to PIK3CA is observed.

morphogenesis normally begins with the descendants of VPC P6.p detaching from the cuticle and forming a symmetric invagination (Fig. 5C) (34). Animals in which the expression of *ras-1*^{WT} had been induced at early L3 largely maintained this pattern (17/20). In contrast, in larvae expressing *ras-1*^{G27dup}, descendants of VPCs P5.p and/or P7.p more frequently detached from the cuticle, resulting in larger and more asymmetric invaginations (10/30). This morphogenesis defect was the earliest detectable effect of the *ras-1*^{G27dup} allele on vulval development, similarly to that previously documented in transgenic lines expressing SHOC2^{S2G} (38).

Genetic interaction between the RAS-1/RRAS mutant and LET-60/RAS was also investigated. While expression of the RAS-1^{G27dup} mutant was able to exacerbate the multivulva

phenotype associated with a hyperactive *let-60* allele (*n1046*), expression of wild-type RAS-1 failed to do so (Table 1). Similarly, a significant, although partial rescue of the VPC induction defect associated with a *let-23/EGFR* hypomorphic allele (*sy1*) was observed in animals expressing the activating RAS-1^{G27dup} mutant, but not in worms expressing the wild-type counterpart (Table 1). Overall, these experiments provided evidence of a positive modulatory role of the RAS-1/RRAS mutant on LET-60/RAS signalling.

DISCUSSION

Mutations of genes coding for proteins with role in RAS signalling and the RAF/MEK/ERK cascade have been identified as the

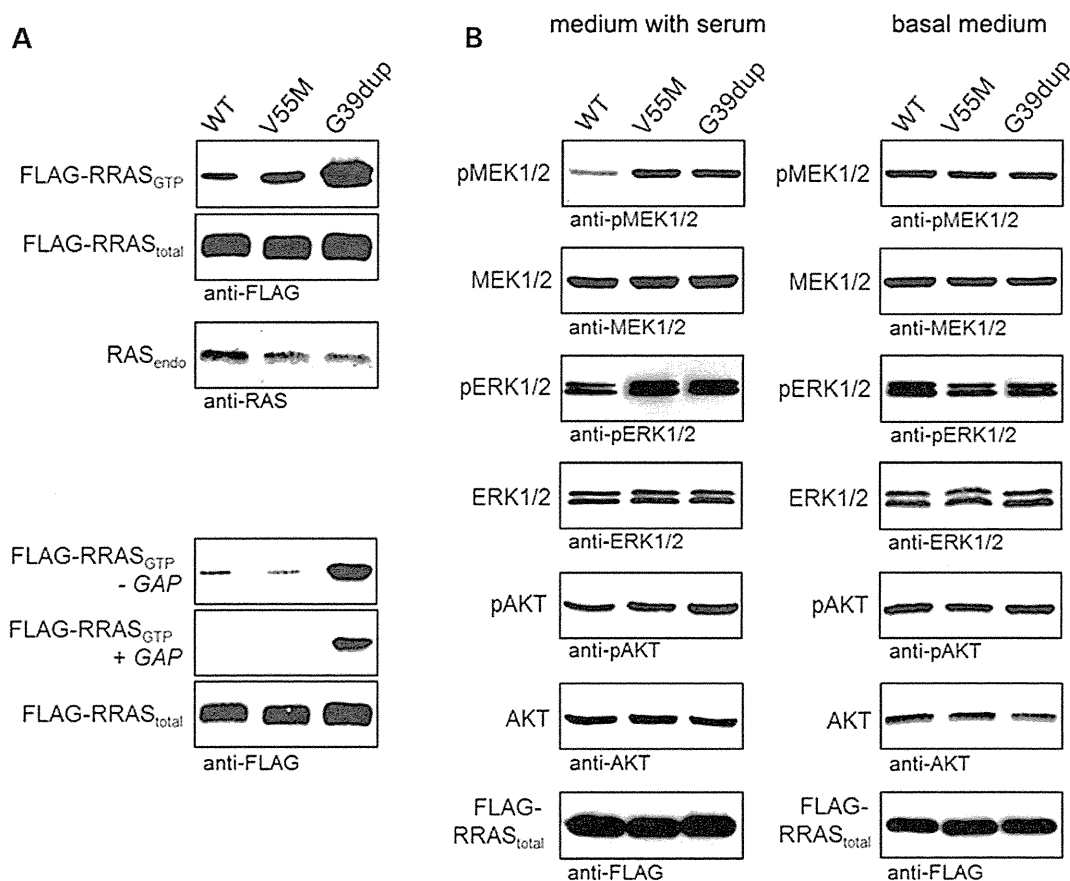


Figure 4. RRAS^{G39dup} and RRAS^{V55M} signalling activities in cells. (A) Determination of GTP-bound RRAS levels in COS-7 cells transiently expressing wild-type or mutant FLAG-tagged RRAS proteins. Assays were performed in the presence of serum (above), and in serum-free conditions (– GAP) or in the presence of the neurofibromin GAP domain (+GAP) (below). RRAS^{G39dup} was predominantly present in the active GTP-bound form and was resistant to GAP stimulation, whereas a slightly increased level of GTP-bound RRAS^{V55M} was observed in the presence of serum. Representative blots of three performed experiments are shown. (B) Determination of MEK, ERK and AKT phosphorylation levels (pMEK, pERK and pAKT) in transiently transfected COS-7 cells cultured in medium with serum (left) or basal medium (right). Expression of each RRAS mutant resulted in variably enhanced MEK, ERK and also partially AKT phosphorylation after stimulation. Total MEK, ERK and AKT in cell lysates are shown for equal protein expression and loading. Expression levels of exogenous, FLAG-tagged RRAS in cell lysates are shown for each experiment. Representative blots of three performed experiments are shown.

molecular cause underlying a group of clinically related developmental disorders, the RASopathies. Here, we used a gene candidacy approach based on large-scale protein–protein interaction/functional network analysis to identify *RRAS* as a novel gene implicated in a condition with features within the RASopathy spectrum. Disease-causing *RRAS* mutations are activating and act by maintaining the GTPase in its GTP-bound active state. Aberrant RRAS function was demonstrated to perturb variably intracellular signal flow through the RAF/MEK/ERK cascade, and to a certain extent also the PI3K/AKT pathway. Of note, these gain-of-function mutations are likely to define a novel leukaemia-prone condition. Consistent with this view, the same class of *RRAS* lesions was identified to occur as acquired somatic event in JMML, characterizing a subset of this myeloproliferative/myelodysplastic disorder with rapid progression to AML.

RRAS shares several biochemical properties with HRAS, NRAS and KRAS, as well as some common function, including

stimulation of cell proliferation, survival and transformation (19,39). Despite these similarities, however, previous observations have emphasized the role of RRAS in cell adhesion, spreading and migration, and its modulatory function on effectors distinct from those used by ‘classical’ RAS proteins (40,41). While PI3K/AKT has been recognized as a major effector pathway of RRAS, only a minor impact on MAPK signalling had been reported (41,42). The present *in vitro* findings provide evidence that disease-associated RRAS mutants enhance the activation of the MAPK cascade, at least in response to specific stimuli. On the other hand, the identification of *RRAS* as a novel disease gene implicated in a RASopathy disorder further emphasizes the relevance of dysregulated signalling controlling cell spreading and migration in certain features of NS (e.g. congenital heart defects and lymphedema) and JMML (leukocyte infiltration in non-haematopoietic tissues) (43–45).

Caenorhabditis elegans studies provided evidence for a genetic interaction between the RAS-1^{G27dup}/RRAS^{G39dup} and

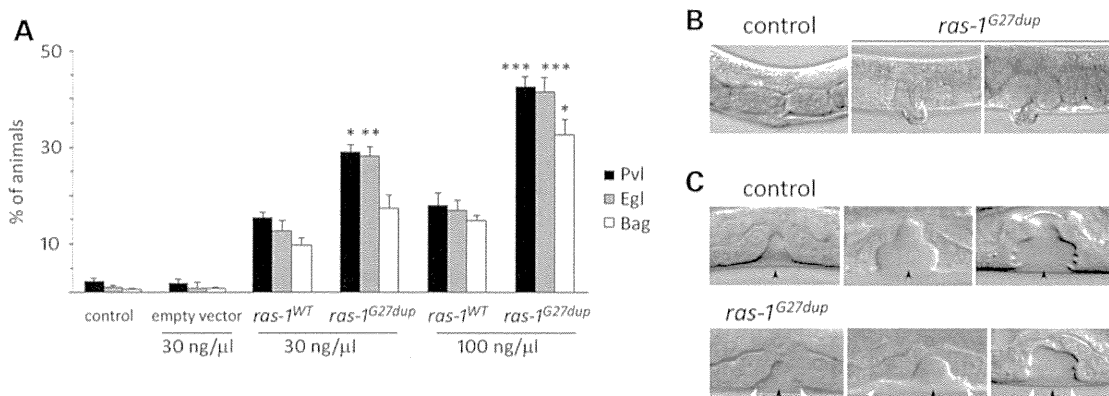


Figure 5. Consequences of *ras-1^{G27dup}* expression on *C. elegans* vulval development. (A) Heat-shock-driven expression of *ras-1^{WT}* and *ras-1^{G27dup}* at early L3 stage results in protruding vulva (Pvl), egg laying defective (Egl) and bag-of-worms (Bag) phenotypes. Isogenic animals that had lost the transgene (control group) and worms expressing the heat shock-inducible vector (empty vector) were subjected to heat shock and scored in parallel for comparison. The dose at which the transgene has been injected is reported at the bottom. Error bars indicate SD of three independent experiments. Asterisks indicate significant differences compared with *ras-1^{WT}* at the corresponding dose of injection ($*P < 0.05$; $**P < 0.005$; $***P < 0.0005$; Fisher's Exact Test). (B) A proper vulva develops in heat-shocked control animals (left), whereas a protruding vulva is observed in heat-shocked *ras-1^{G27dup}* young adults (middle) and adult worms (right). (C) Nomarski images of vulval precursor cells in late L3 (left), early L4 (middle) and mid-late L4 (right) stages from synchronized animals heat-shocked at early L3. In control animals ($N = 48$), only P6.p descendants invaginate (upper panel), whereas in 10 of 30 analysed *ras-1^{G27dup}*-expressing worms, P5.p and/or P7.p descendants also detach from the cuticle, generating asymmetric invaginations (lower panel). Black arrowheads point to P6.p descendant invagination, whereas white arrowheads point to P5.p and P7.p descendant invagination. Anterior is to the left and dorsal is up, in all images.

LET-60/RAS *in vivo*. Specifically, expression of the RAS-1 mutant protein was able to rescue, in part, the VPC induction defect resulting from a hypomorphic LET-23 mutant and enhanced the multivulva phenotype associated with a LET-60 gain-of-function genetic background. No impact of wild-type RAS-1/RRAS expression was observed in both models. We also observed that worms expressing *ras-1^{G27dup}* displayed abnormal vulval morphogenesis (protruding vulva), possibly resulting from aberrant morphogenetic movements of the VPC descendant cells. Of note, we observed an equivalent phenotype in transgenic lines expressing SHOC2^{S2G} (38) and a PTPN11/SHP2 gain-of-function mutant (our unpublished data), suggesting functional equivalence of these mutants. Genetic studies support the view that these vulva defects arise, in part, through perturbation of signalling mediated by the RHO-related GTPase, RAC, which plays a critical role in vulval morphogenesis (37). This finding is in line with the established role of RRAS on RAC signalling (40,41) and with preliminary data indicating enhanced migration and chemotactic capabilities in cells stably expressing the disease-associated RRAS mutants (our unpublished data).

The biochemical characterization of disease-associated RRAS mutations provided strong evidence for the existence of distinct structural and mechanistic effects resulting in an overall enhancement of RRAS signalling. Function of RAS family proteins in signal transduction is controlled by two events, the GDP/GTP exchange and GTP hydrolysis. Any perturbation of these processes can affect dramatically the fine-tuned balance of the GTPase interaction with effectors and signal output. The majority of gain-of-function mutations affecting RAS proteins, including those contributing to oncogenesis, trigger the accumulation of these GTPases in the active state by impairing intrinsic GTPase activity, and/or conferring resistance to GAPs (17). This is also the case of two of the three mutations identified in this

study, p.Gly39dup and p.Gln87Leu, the latter corresponding to the p.Gln61Leu in RAS proteins (present study and ref. 18,19). The characterization of the biochemical behaviour of RRAS^{G39dup}, however, also demonstrated a dramatic increase in both the intrinsic and GEF-catalysed nucleotide exchange as a process contributing to the accumulation of this mutant in its GTP-bound state. Aberrant GEF-accelerated nucleotide exchange dynamics was identified as the event driving functional dysregulation in the RRAS^{V55M} mutant, which was documented to be hyper responsive to GEF stimulation, but retained stimulus-dependency. Remarkably, the RRAS^{G39dup} and RRAS^{V55M} mutants were demonstrated to exhibit a diverse binding behaviour to effectors suggesting a differential impact of mutations on downstream signalling cascades, including PI3K/AKT and RALGDS/RAL, whose biological significance and impact, however, require further studies.

The clinical phenotype of the two subjects with germline RRAS mutations was reminiscent of NS. The individual with the Gly³⁹ duplication displayed pulmonic stenosis, reduced growth, café-au-lait spots, mild motor delay and low-set ears, which recur in NS (5). Facial features, however, were distinctive, and not typical of NS. In contrast, the patient heterozygous for the p.Val55Met substitution exhibited a very mitigated phenotype characterized by suggestive facial characteristics (triangular face, downslanting palpebral fissures and low-set ears), low posterior hairline, broad chest and borderline cognitive abilities, without cardiac involvement or defective growth, indicating that clinical features associated with RRAS mutations might be quite subtle. Of note, the milder phenotype associated with the p.Val55Met change is consistent with the weaker perturbing effect of the RRAS^{V55M} mutant on MAPK and PI3K/AKT signalling compared with the RRAS^{G39dup} protein. Additional information on the spectrum of germline RRAS mutations, their associated phenotype and their functional impact on signalling,

Table 1. Vulva phenotypes in *C. elegans* mutant strains expressing wild-type RAS-1 or the disease-associated RAS-1^{G27dup} mutant

Genotype	Transgene	N	Muv (%)	Vul (%)	Pvl (%)	N	P6.p induction (%)
wild-type	none	207	0	0	1.0	48	100
<i>let-60(n1046)</i>	none	201	77.9	–	0.5	50	100
<i>let-60(n1046)</i>	<i>ras-1^{WT}</i>	244	76.4	–	2.8	43	100
<i>let-60(n1046)</i>	<i>ras-1^{G27dup}</i>	231	87.1 ^a	–	3.0	50	100
<i>let-23(sy1)</i>	none	194	–	87.8	3.6	178	13.4
<i>let-23(sy1)</i>	<i>ras-1^{WT}</i>	169	–	84.3	4.1	156	14.0
<i>let-23(sy1)</i>	<i>ras-1^{G27dup}</i>	282	–	83.3	10.3 ^c	128	24.2 ^c

Strains: *let-60(n1046)* is a gain-of-function allele of *let-60* (ortholog of the human *HRAS*, *KRAS* and *NRAS* genes); *let-23(sy1)* is a hypomorphic allele of *let-23* (ortholog of the human *EGFR* gene). *ras-1^{WT}* and *ras-1^{G27dup}* indicate *hsp-16.41::ras-1^{WT}*- and *hsp-16.41::ras-1^{G27dup}*-containing constructs injected at 100 ng/μl, respectively. After each cross, isogenic worms that had lost the transgene were cloned separately and used as controls.

Animals were grown at 20°C and heat-shocked in parallel at early L3 stage. N indicates the number of animals scored. Multivulva (Muv), vulvaless (Vul) and protruding vulva (Pvl) phenotypes are expressed as percentage of worms with ectopic pseudovulvae, animals lacking a vulva and adults with a protruding vulva, respectively. Induction of vulval cell fate is expressed as percentage of P6.p that has been induced to invaginate.

In all comparisons, P-values were calculated using two-tailed Fisher's exact test.

^aSignificantly different from *let-60(n1046)* ($P < 0.02$).

^bSignificantly different from *let-23(sy1)* ($P < 0.01$) and *let-23(sy1);ras-1^{WT}* ($P < 0.02$).

^cSignificantly different from *let-23(sy1)* ($P = 0.02$) and *let-23(sy1);ras-1^{WT}* ($P < 0.05$).

however, is necessary to establish clinically relevant genotype–phenotype correlations.

JMML is a clonal myeloproliferative/myelodysplastic disorder of childhood characterized by overproduction of immature myeloid cells that variably retain the capacity to differentiate. Upregulation of RAS/MAPK signalling owing to germline and somatic mutations in *PTPN11*, *NRAS*, *KRAS*, *NF1* and *CBL* is a major event implicated in this malignancy (13,46,47). Our data document that upregulated *RRAS* function represents a novel event contributing to JMML pathogenesis and/or disease progression. Notably, somatic *RRAS* mutations co-occurred with acquired *NRAS* lesions in atypical JMML characterized by late onset and rapid progression to AML. While JMML is generally an aggressive malignancy, a subset of *NRAS/KRAS* mutation-positive patients has been reported to exhibit a mild course, with spontaneous remission despite the *RAS*-mutated clone persisting for years (48–50, our unpublished data). This suggests that in some instances, certain *NRAS* mutations are not sufficient to support full leukaemogenesis, requiring synergism with a second RAS signalling targeting event. In line with this view, *NRAS* mutations have been documented to co-exist with defects in other RASopathy genes (e.g. *PTPN11*) in some cases resulting in a particularly aggressive disease resembling AML with myelodysplasia-related changes (51,52), as that observed in the present cases. Other studies, however, are required to appreciate more precisely the role of enhanced *RRAS* function in leukaemogenesis as well as its clinical relevance in haematological malignancies.

In conclusion, our findings document that germline activating mutations in *RRAS* underlie a condition within the RASopathy family that may resemble NS phenotypically. In the examined cohorts, *RRAS* lesions were found to account for only a small portion of cases, which might be related to their severe consequences on embryonic/foetal development and/or to the biased selection of the subjects included in this study. Based on the present findings, however, *RRAS* mutations are expected to be more common among subjects with clinical features only partially overlapping NS, and particularly in patients with syndromic JMML/AML not associated with mutations in the *PTPN11*, *NF1*, *CBL*, *KRAS* and *NRAS* genes. While further efforts are

required to characterize more precisely the clinical impact of germline and somatic mutations affecting *RRAS*, our findings suggest an unpredicted role of this GTPase in development and haematopoiesis. Consistent with the recent identification of *RITI* as disease gene implicated in a significant proportion of NS (9), our findings further extend the concept of 'RASopathy gene' to a transducer whose dysregulated function perturbs signal flow through the MAPK cascade but does not belong to the core RAS/MAPK signalling cassette.

MATERIALS AND METHODS

Selection of RASopathy candidate genes

A web-based tool, Genes2FANs (<http://actin.pharm.mssm.edu/genes2FANs>), using a large-scale protein–protein interaction network coupled to a panel of functional association networks (FANs) was utilized to build a subnetwork connecting proteins to the known RASopathy genes (i.e. *PTPN11*, *SOS1*, *NF1*, *SPRED1*, *CBL*, *NRAS*, *KRAS*, *HRAS*, *RAF1*, *BRAF*, *SHOC2*, *MAP2K1* and *MAP2K2*), as seed proteins. Gene Ontology (biological process tree), mammalian phenotype browser, and Connectivity Map (drug-associated gene expression signatures), ChEA and TRANSFAC (transcription factor networks) databases were selected to construct the functional subnetworks utilized for prioritization of candidates (15). The programme allows to calculate z-scores for intermediate nodes (i.e. candidates), which are ranked based on their connections to the seed proteins.

Subjects and mutation analysis

Three cohorts of patients were considered in the study. A first group including 96 subjects with clinical features within the RASopathy spectrum and without mutation in previously identified RASopathy genes (i.e. *CBL*, *PTPN11*, *SOS1*, *KRAS*, *HRAS*, *NRAS*, *RAF1*, *BRAF*, *SHOC2*, *MAP2K1* and *MAP2K2*) was screened for a selected panel of candidates. A second cohort including 408 subjects with NS or a closely related phenotype previously tested negative for mutations in a heterogeneous subset

of RASopathy genes was scanned for *RRAS* mutations. All subjects included in this cohort had been screened for mutations in *PTPN11*, *SOS1* and *RAF1* genes. In both cohorts, the clinical diagnosis was made on the basis of standardized clinical criteria assessed by experienced clinical geneticists and paediatricians. Clinical features for the majority of subjects satisfied diagnostic criteria reported for NS, LEOPARD syndrome and cardiofaciocutaneous syndrome (53–57), but individuals who lacked sufficient features for a definitive diagnosis were also included. *RRAS* mutation analysis was also carried out on a cohort including 110 subjects with non-syndromic JMML that had prospectively been collected and genotyped (58). Mutation screening was performed on the entire *RRAS* coding sequence and flanking intronic stretches (NC_000019.10, 49635295..49640143, complement; NM_006270.3; NP_006261.1) on genomic DNA extracted from circulating leukocytes (cohorts I, II and III) or bone marrow aspirates (cohort III) by denaturing high-performance liquid chromatography (DHPLC) (3100 or 3500HT WAVE DNA fragment analysis system, Transgenomic, Omaha, NE, USA) and/or direct bidirectional sequencing (ABI Prism 3130, 3730 and 3500 Genetic Analyzers; Applied Biosystems, Foster City, CA, USA). Primer pairs, PCR and DHPLC conditions are available upon request. dbSNP137 (http://www.ncbi.nlm.nih.gov/projects/SNP/snp_summary.cgi), HapMap (rel.27) (<http://hapmap.ncbi.nlm.nih.gov/>) and 1000 Genomes (<http://www.1000genomes.org/>) databases were used to annotate the identified sequence variants. SIFT (<http://sift.jcvi.org/>), PolyPhen-2 (<http://genetics.bwh.harvard.edu/pph2/>) and MutationTaster (<http://www.mutationtaster.org/>) were used to predict the functional impact of the identified variants. Paternity was confirmed by STR genotyping, using the PowerPlex 16 System (Promega). DNA from leukocytes, hair bulb cells, bone marrow aspirates and skin fibroblasts was extracted using standard protocols. DNA specimens were collected under Institutional Review Board-approved protocols. Informed consent for DNA storage and genetic analyses was obtained from all subjects. Permission was obtained to publish picture of patient 9802, whereas subject NS1166 denied consent for picture publication.

Exome sequencing

Targeted enrichment and massively parallel sequencing were performed on genomic DNA extracted from circulating leukocytes and fibroblasts of patient 9802. Exome capture was carried out using the SureSelect Human All Exon V4+UTRs (Agilent), and sequencing with a HiSeq2000 instrument (Illumina). Image analysis and base calling were performed using the Real Time Analysis (RTA) pipeline v. 1.14 (Illumina). Paired-end reads alignment to the reference human genome (UCSC GRCh37/hg19) and variant calling were carried out using the CASAVA v. 1.8 pipeline (Illumina). Variant annotation, SNP filtering (dbSNP135, 1000 Genomes, HapMap and IntegraGen Exome databases) and patient-matched germline variant filtering were attained using an in-house pipeline by IntegraGen (Evry, France).

Molecular dynamics analyses

Starting coordinates for MD simulations were obtained from the *RRAS* crystallographic structure in complex with GDP and

Mg²⁺ (PDB: 2FN4; RCSB Protein Data Bank, <http://www.rcsb.org/pdb/home/home.do>). The *N*-terminus and *C*-terminus of *RRAS*, absent in the crystal, were not considered in simulations. Deep View software was used to add atoms missing in the PDB file, belonging to residues 31, 96, 114, 121 and 192 as well as to substitute residue 55 (simulation of the p.Val55Met mutant) (59). All MD simulations were performed with GROMACS 4.5 package, by using the GROMOS96 43a1 force field parameters for the protein. Parameters for GDP were taken from the GROMACS website (<http://www.gromacs.org>). Simulations were performed as previously described (60,61), except for some details. Briefly, the proteins were initially placed in a dodecahedral box, solvated with ~6700 SPC water molecules, and six Na⁺ ions were added to neutralize the protein charge. Following initial energy minimization and a 100-ps MD run, during which the protein atoms were position restrained, the temperature of solute and solvent was raised from 50 to 300 K in a stepwise manner. 200-ns-long simulations were performed for wild-type *RRAS* and the RASopathy causative mutant. The particle mesh Ewald method was used to evaluate electrostatic interactions (62), whereas a cut-off scheme was employed for Van der Waals interactions. Temperature and pressure were kept constant at 300 K and 1 bar by using the Berendsen weak-coupling method (63), using separate temperature baths for protein–GDP complex and solvent, with a relaxation time of 0.1 ps for temperature and 1 ps for pressure. A time step of 2 fs was employed. Root mean square deviations were calculated according to standard definitions. UCSF Chimera (<http://www.cgl.ucsf.edu/chimera/>) was used for molecular graphics and structures superposition, by using the MatchMaker option.

Biochemical and functional characterization of *RRAS* mutants

The generation of constructs, and preparation and purification of proteins were as previously described (64). The intrinsic activities of the RAS proteins, their modulation by GEFs and GAPs and their interaction with different effector proteins were determined as described earlier (65,66). Dissociation of mantGDP from RAS proteins (0.1 μM) was measured in the presence of 20 μM GDP in 30 mM Tris–HCl, pH 7.5, 10 mM KH₂PO₄/K₂HPO₄, 5 mM MgCl₂, 3 mM dithioerythritol (DTE), at 25 °C, using a Perkin Elmer fluorimeter at 366 nm (excitation wavelength) and 450 nm (emission wavelength). Observed rate constants (*k*_{obs}) of dissociation were obtained by single exponential fitting of the data. GEF-accelerated mantGDP dissociation from RAS proteins (0.1 μM) was measured as mentioned earlier, in the presence of the catalytic domain of SOS1, Cdc25 (5 μM), using stopped-flow instrument.

The intrinsic GTPase reaction was performed by mixing 70 μM nucleotide-free RAS proteins (HRAS, *RRAS*^{WT}, *RRAS*^{V55M} and *RRAS*^{G39dup}) with 50 μM GTP in 30 mM Tris–HCl, pH 7.5, 10 mM KH₂PO₄/K₂HPO₄, 10 mM MgCl₂, 3 mM DTE, at 25 °C, using HPLC assay as previously described (67). Samples were taken at different time points and analysed by HPLC for their GDP and GTP contents to determine the relative GTP content [(GTP)/(GDP + GTP)]. Intrinsic GTP hydrolysis *k*_{obs} of proteins were obtained by single exponential fitting of the data. For determination of GAP (neurofibromin, residues